

PAPER • OPEN ACCESS

Laser-induced graphene on cross-linked sodium alginate

To cite this article: T Vićentić *et al* 2024 *Nanotechnology* **35** 115103

View the [article online](#) for updates and enhancements.

You may also like

- [UV-Ozone Treated Modified Laser-Induced Graphene Based Electrochemical Sweat Sensor](#)
Sudipta Choudhury, Gourav Bhattacharya and Susanta Sinha Roy
- [Direct-write formation of integrated bottom contacts to laser-induced graphene-like carbon](#)
Richard Murray, Orla O'Neill, Eoghan Vaughan et al.
- [Highly responsive screen-printed asymmetric pressure sensor based on laser-induced graphene](#)
Jiang Zhao, Jiahao Gui, Jinsong Luo et al.

PRIME
PACIFIC RIM MEETING
ON ELECTROCHEMICAL
AND SOLID STATE SCIENCE










HONOLULU, HI
Oct 6–11, 2024

Abstract submission deadline:
April 12, 2024

Learn more and submit!

Joint Meeting of
The Electrochemical Society
•
The Electrochemical Society of Japan
•
Korea Electrochemical Society

Laser-induced graphene on cross-linked sodium alginate

T Vićentić^{1,*} , I Greco² , C S Iorio² , V Mišković³ ,
D Bajuk-Bogdanović⁴ , I A Pašti⁴ , K Radulović¹, S Klenk⁵,
T Stimpel-Lindner⁵ , G S Duesberg⁵  and M Spasenović¹ 

¹ Center for Microelectronic Technologies, Institute of Chemistry, Technology and Metallurgy, University of Belgrade, Belgrade, Serbia

² Center for Research and Engineering in Space Technologies (CREST), Université Libre de Bruxelles, Bruxelles, Belgium

³ Nearlab, Department of Electronics, Information, and Bioengineering, Politecnico di Milano, Milano, Italy

⁴ University of Belgrade—Faculty of Physical Chemistry Belgrade, Serbia

⁵ Institute of Physics, EIT 2, Faculty of Electrical Engineering and Information Technology, University of the Bundeswehr Munich & SENS Research Center, Neubiberg, Germany

E-mail: teodora.vicentic@ihm.bg.ac.rs

Received 25 August 2023, revised 15 November 2023

Accepted for publication 10 December 2023

Published 29 December 2023



CrossMark

Abstract

Laser-induced graphene (LIG) possesses desirable properties for numerous applications. However, LIG formation on biocompatible substrates is needed to further augment the integration of LIG-based technologies into nanobiotechnology. Here, LIG formation on cross-linked sodium alginate is reported. The LIG is systematically investigated, providing a comprehensive understanding of the physicochemical characteristics of the material. Raman spectroscopy, scanning electron microscopy with energy-dispersive x-ray analysis, x-ray diffraction, transmission electron microscopy, Fourier-transform infrared spectroscopy and x-ray photoelectron spectroscopy techniques confirm the successful generation of oxidized graphene on the surface of cross-linked sodium alginate. The influence of laser parameters and the amount of crosslinker incorporated into the alginate substrate is explored, revealing that lower laser speed, higher resolution, and increased CaCl₂ content leads to LIG with lower electrical resistance. These findings could have significant implications for the fabrication of LIG on alginate with tailored conductive properties, but they could also play a guiding role for LIG formation on other biocompatible substrates.

Supplementary material for this article is available [online](#)

Keywords: laser-induced graphene, alginate, nanobiotechnology, graphene synthesis, biocompatible materials, graphene characterization

1. Introduction

Ever since the discovery of graphene in 2004, the exceptional physical and chemical properties of this material have motivated scientists worldwide to search for novel techniques for its production. Micromechanical exfoliation is the method that led to the discovery of graphene. However, pristine graphene flakes produced this way are only suitable for laboratory-scale testing of fundamental properties of this

* Author to whom any correspondence should be addressed.

material, and small-scale proof-of-concept demonstrations [1, 2]. An alternative production method, potentially compatible with mass production is chemical vapor deposition (CVD). This method yields high-quality large area graphene layers deposited on copper or nickel substrates but requires subsequent transfer to substrates that are useful for applications. However, the transfer process often results in the formation of defects, cracks and wrinkles, leading to a reduction in quality [3–5]. Another technique for obtaining large quantities of graphene is liquid phase exfoliation (LPE). The method is based on the exfoliation of graphene flakes from graphite dispersed in organic solvents or water in assistance of surfactants or polymers. Although graphene flakes obtained with LPE are small compared to the ones obtained by CVD or micromechanical exfoliation, this method is suitable for a variety of applications, especially when coupled with reliable methods of flake deposition into thin films on solid substrates [6, 7]. However, LPE typically has low efficiency requiring extensive ultrasonication, which fractures the graphene flakes. In addition, graphene obtained with LPE is plagued by chemical impurities, and the method is inherently limited by the choice of solvents [8, 9]. Yet another graphene preparation approach that is frequently used involves the oxidation of graphite, which is then exfoliated in a liquid to produce graphene oxide (GO) [10, 11], which can be reduced to obtain graphene. This method introduces many defects in the carbon lattice that degrade the electronic properties of graphene. Moreover, this method requires the use of strongly oxidizing and reducing agents, which leads to safety and environmental concerns. The mentioned techniques have limitations in terms of efficiency, time consumption, and environmental impact.

The use of lasers in graphene production opens new possibilities. For example, laser-mediated explosive synthesis and transfer (LEST) has been used to generate and transfer graphene flakes and nanohybrids onto a substrate [12], and laser-induced backside transfer (LIBT), has demonstrated the potential for the precise and efficient transfer of monolayer graphene and other 2D materials [13]. In 2014 it was discovered that 3D porous graphene can be produced by using a CO₂ infrared laser to write directly on commercial polyimide (PI) precursor films under ambient conditions [14]. Graphene made with this method possesses interesting properties, such as a high surface-to-volume ratio, mechanical and thermal stability and good conductivity. This straightforward fabrication is easily accessible, since it does not require expensive tools, special ambient conditions or post-fabrication treatment. Over time, the range of precursor materials for laser-induced graphene (LIG) production has been broadened to different types of carbon containing substrates. A variety of commercial polymers have been investigated to achieve and optimize the production of LIG. Polymers similar in structure to PI and polyetherimide (PEI) such as polysulfone, polyethersulfone and sulfonated polyether ether ketone are found to be suitable for LIG synthesis [15, 16]. Besides pure polymers, the conversion of metal/plastic composites into LIG has also been investigated. Direct scribing on metal-complex-containing PI film leads to the formation of

nanoparticles embedded in porous graphene [17]. PI sheets containing boric acid resulted in the formation of boron-doped porous graphene [18]. Among naturally occurring materials, examples that showed good conversion to LIG include wood, lignin, coconut and potato surface [19–21]. These materials are interesting candidates as precursors for LIG because they are natural and environmentally friendly.

In general, biopolymers seem to be optimal candidates for LIG precursors, because of their large variety, rich carbon content, biocompatibility and wide availability. One particularly interesting biopolymer is sodium alginate (SA). In general, alginate is a linear polysaccharide composed of D-mannuronate and L-guluronate residues linked in various degrees through an $\alpha(1,4)$ linkage [22]. This material is extracted from brown algae species like *Laminaria hyperborea* and *Lessonia*, which are commonly found in coastal areas worldwide [23–25]. SA is a non-toxic, biodegradable, biocompatible and cost-effective material [22]. In the presence of a crosslinker such as calcium chloride, SA can create a hydrogel. The crosslinking process enhances the stability and viscosity of the sodium alginate, making it suitable for a range of applications. Some of the applications include drug and protein delivery, wound dressing, tissue regeneration and cartilage growth promotion [26]. Despite its excellent properties and numerous applications, this material has not been previously reported as a precursor for laser induction of graphene. Direct laser induction of graphene on the surface of sodium alginate would open possibilities of inscribing electric circuits such as sensors on biological structures with little effort, which would propel the use of wearable LIG-based sensors [27–29]. This study demonstrates the production of graphene on cross-linked sodium alginate (CL-SA) substrates through laser induction, as illustrated in figure 1. In addition, we provide a comprehensive analysis of the physicochemical properties of the produced LIG under different laser parameters, using Raman spectroscopy, scanning electron microscopy (SEM) with energy-dispersive x-ray analysis (EDS), x-ray diffraction (XRD), transmission electron microscopy (TEM), Fourier-transform infrared spectroscopy (FTIR), and x-ray photoelectron spectroscopy (XPS). We find that all methods confirm formation of graphene on the CL-SA surface. LIG on CL-SA has potential applications in bioelectronics, including medical wearables.

2. Experimental

2.1. Alginate synthesis and graphene induction

Sodium alginate (SA) and calcium chloride dihydrate (CaCl₂) were purchased from Sigma Aldrich (9005-38-3). For this work, three sets of samples were prepared with three different concentrations of the CaCl₂ crosslinker. SA was dissolved in distilled water at 4% (w/v) concentration. The solution was stirred for 2 h at 40 °C until it became homogeneous and degassed for 2 h to eliminate air bubbles. The solution was then ionically crosslinked by immersing it in a bath of CaCl₂ water solution for 1 h to ensure complete crosslinking. The

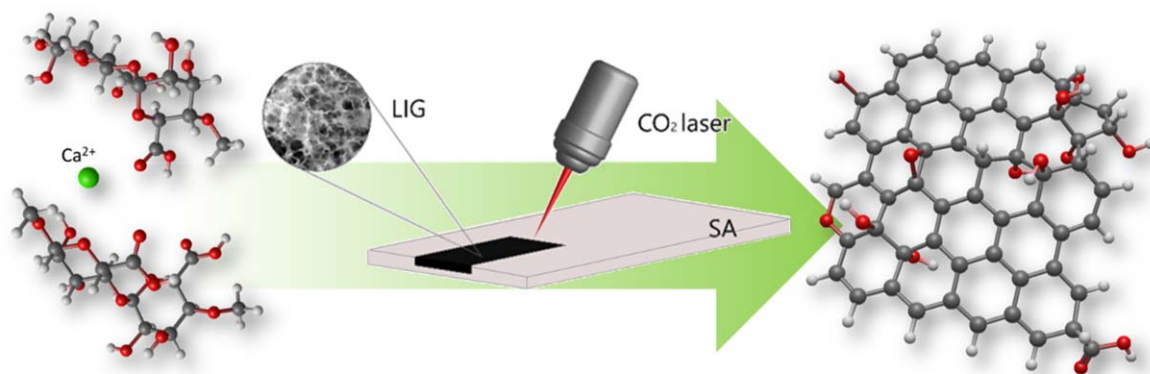


Figure 1. Schematic view of laser induction of graphene on CL-SA. The CL-SA, depicted on the left side of the image, is exposed to laser radiation (middle), which converts a thin layer of CL-SA into LIG (right).

CaCl₂ water solution was prepared by dissolving the CaCl₂ powder in distilled water and stirring for 15 min until the salt was completely dissolved. Dried alginate samples had a thickness of ~0.1 mm. Prepared CL-SA samples were used as precursors for the laser-induced formation of graphene. The laser used to produce LIG was a DBK FL-350.

2.2. LIG characterization

Raman spectra of the samples were recorded with a DXR Raman microscope (Thermo Fisher Scientific, Waltham, MA, USA). The samples were excited with a diode laser at a wavelength of 532 nm and a power of 10 mW, focused on a 2.1 μm spot on the surface. Spectra were obtained as averages of three measurements from different positions on each sample (10 exposures, 10 s each per position). The recorded Raman spectra were treated to correct the fluorescence background using a 5th-order polynomial baseline correction method built-in the Omnic software (OMNIC for Dispersive Raman 9.2.41.). FTIR of CL-SA and LIG were recorded in reflectance mode with a Nicolet™ iN10 Infrared Microscope and FTIR spectrophotometer (Thermo Fisher Scientific, Waltham, MA, USA). SEM with EDS was done with a PhenomProX scanning electron microscope (Phenom, Thermo Fisher Scientific, Waltham, MA, USA). XRD analysis was carried out on a D8 Advance Eco diffractometer with Cu Kα radiation ($\lambda = 0.15406$ nm, Bruker, Germany). The FEI Talos F200X microscope (Thermo Fisher Scientific, Waltham, MA, USA) operating at 200 kV was utilized to conduct both conventional and high-resolution transmission electron microscopy (TEM/HRTEM) analysis. To prepare a sample for TEM analysis, the LIG powder peeled off the substrate was dispersed in ethanol using ultrasound. Once dispersed, a small amount of the solution was deposited onto a carbon-coated copper grid and allowed to dry in ambient air. For XPS measurements, a PHI VersaProbe III instrument equipped with a micro-focused monochromatic Al Kα source (1486.6 eV) and dual beam charge neutralization is used. Core level spectra are recorded with PHI SmartSoft VersaProbe software and processed with CasaXPS. Binding energies are referenced to the adventitious carbon signal at 284.8 eV. After subtraction of a Shirley type background, the spectra are

fitted with Gaussian–Lorentzian peak shapes. Four-point measurements were conducted using a Keithley 2450 SMU device to obtain sheet resistance values of LIG samples. The probes were spaced 3 mm apart.

3. Results and discussion

The laser power was set to 14% (8.4 W of the total available 60W), which is equivalent to an irradiance of 47 kW cm⁻². This observed optimal irradiance is 20%–25% lower than the optimal value for polyimide (PI), which is the traditional material for LIG formation. Even with pulsed lasers, a higher threshold irradiance was observed on polyimide [30], which indicates that CLSA is more easily converted to graphene than PI. Laser power below this threshold does not lead to graphene induction, while higher power causes substrate degradation. The effects of varying laser power are depicted in the optical images of the resultant samples in figures 2(a)–(c). The remaining two laser parameters, speed and resolution, were varied to analyze their impact on the properties of LIG. The effect of changing laser scanning speed was investigated in the range from 100 to 900 mm s⁻¹. The sample produced with the lowest speed is shown in figure 2(d), while figure 2(f) shows the effect that the highest laser scanning speed has on sample appearance. It is evident that in these two cases the produced LIG is not homogeneous. Conversely, figure 2(e) illustrates an example with moderate speed (300 mm s⁻¹), displaying a homogeneous LIG film. Laser resolution was varied between 500 and 1400 DPI. Figure 2(g) depicts a film made with low resolution, demonstrating that lower resolution results in inhomogeneous graphene films. Medium and higher laser resolutions (figures 2(h) and figure (i)) result in continuous, uniform LIG films. The complete set of the studied laser parameters is provided in table 1. Successful graphenization results in samples that are black and opaque. This is due to the fact that LIG is on the order of 8 μm thick [27]. Hence, as opposed to thinner forms of graphene, LIG cannot be characterized with UV–vis transmittance spectroscopy to determine material thickness.

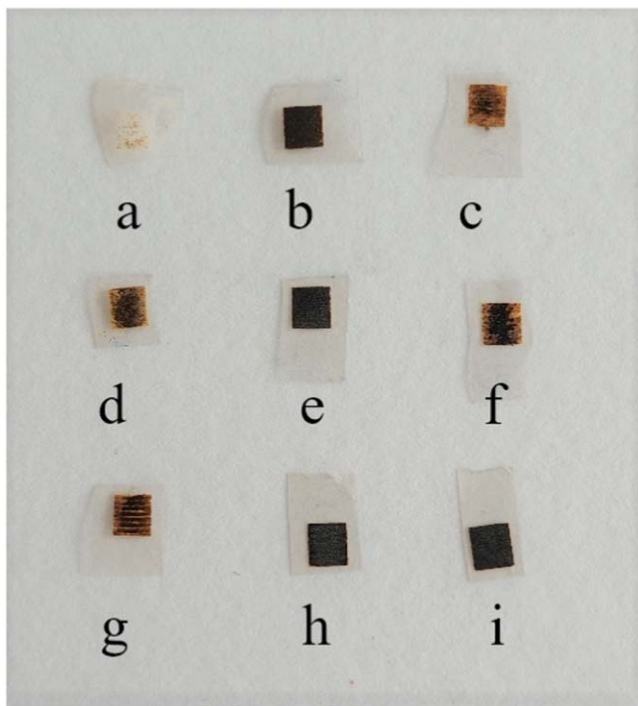


Figure 2. Optical images of LIG samples produced on CL-SA with 15% CaCl_2 and different laser parameters. (a) Power < 8.4 W, scanning speed = 400 mm s^{-1} , resolution = 800 DPI, (b) optimal power (8.4 W), scanning speed = 400 mm s^{-1} , resolution = 800 DPI, (c) power > 8.4 W, scanning speed = 400 mm s^{-1} , resolution = 800 DPI, (d) power = 8.4 W, scanning speed = 100 mm s^{-1} , resolution = 800 DPI, (e) power = 8.4 W, scanning speed = 450 mm s^{-1} , resolution = 800 DPI, (f) power = 8.4 W, scanning speed = 750 mm s^{-1} , resolution = 800 DPI, (g) power = 8.4 W, scanning speed = 300 mm s^{-1} , resolution = 500 DPI, (h), power = 8.4 W, scanning speed = 300 mm s^{-1} , resolution = 800 DPI, and (i) power = 8.4 W, scanning speed = 300 mm s^{-1} , resolution = 1100 DPI. The observed threshold power of 8.4 W corresponds to an irradiance of 47 kW cm^{-2} .

3.1. Raman spectroscopy

The Raman spectrum of LIG on CL-SA (figure 3(a)) exhibits typical features of graphene. Strong D and G bands occur at 1335 cm^{-1} and 1593 cm^{-1} , respectively. The G peak indicates the presence of sp^2 carbon atoms, whereas the D peak indicates the presence of defects. The 2D region ($2250\text{--}3000 \text{ cm}^{-1}$) is well-developed, and the peak at 2700 cm^{-1} originates from second-order zone boundary phonons [31, 32]. The Raman spectra of samples with different concentrations of CaCl_2 , shown in figure 3(b), contain the characteristic peaks, regardless of the quantity of cross-linker. In figures 3(c) and (d) we demonstrate the effects of varying laser parameters. From figure 3(c) it is apparent that at low scanning speed, the G peak intensifies, the ratio of intensities of the D and G peaks (I_D/I_G) changes, and the 2D peak is less pronounced. Such an effect of low scanning speed is expected since the laser irradiates the substrate locally for longer time periods when moving slower, causing degradation of the substrate. From figure 3(d), we conclude that the laser resolution does not impact the quality of graphene.

Detailed deconvolution for the Raman spectra depicted in figure 3 is presented in figure 4. We have fitted the LIG spectra to five functions: three pseudo-Voigt and two Gaussian [33]. Figure S1 shows an example of the deconvoluted spectrum of LIG. Table S1 of the Supporting Information presents band parameters obtained from the fit process.

The relationship between the positions of the D and G bands with laser scanning speed and resolution is illustrated in figures 5(a) and (b), respectively. With an increase in scanning speed, the spectral position of the G band shows a slight shift towards higher values, whereas an increase in laser resolution results in a slight shift towards lower values. Conversely, the position of the D band shifts to lower values with increased scanning speed, but it remains unchanged when the laser resolution is increased. Plotting the I_D/I_G ratio can be used to estimate the crystalline size of LIG [34]. Figures 5(c) and (d) display the changes in the I_D/I_G ratio concerning laser scanning speed and resolution, respectively. The I_D/I_G ratio reaches a maximum at high scanning speed and low resolution, indicating that the crystalline size of LIG is maximized at 800 mm s^{-1} scanning speed and 500 DPI laser resolution. The D^* band has been associated with a disordered graphitic lattice found in soot due to the presence of sp^3 bonds [35]. Consequently, an investigation into the variations in D^* band intensity was conducted using different laser parameters. Figure 5(e) illustrates the plot of the D^* band intensity, normalized to the intensity of the G band, as a function of oxygen content. It can be noted that samples produced with low scanning speed and high-resolution display reduced D^* band intensity. According to the interpretation of Vollebregt *et al*, the D^* band is related to amorphous phases since its intensity decreases with the increase of the crystallinity [36]. The D^* band intensity normalized to the intensity of the G band is related to ordering length L_a , as an indicator of the crystallinity. The I_{D^*}/I_G ratio decreases as the crystallinity increases in the case of lower scanning speed values, in the range from 100 to 450 mm s^{-1} . The lowest crystallinity is observed when applying scanning speed 500 mm s^{-1} and very low resolution = 500 DPI. Since the laser spot diameter at focus is $\sim 150 \text{ mm}$, there is significant overlap between laser passes even at the lowest resolution setting. At 500 DPI, the spot passes about 3 times over the same area of the CL-SA, whereas at 1100 DPI the spot passes about 6 times over the same area. It is evident, especially from figure 5(f), that the crystallinity (level of graphenization) rises with resolution, which results from a higher number of laser passes over any given area. The dependence of crystallinity on the number of passes has also been observed with LIG on PI [37]. To compare the levels of structural order among the LIG samples presented in figure 3, we have depicted the relationship between the full width at half maximum (FWHM) of the D and G peaks and the material production parameters in figure S3. A decrease in the FWHM of the G peak signifies the presence of larger sp^2 grains. Therefore, the variations shown in figure S3a indicate the formation of better-defined graphene domains in the case of the polymer precursor with higher CaCl_2 content. In terms of varying laser

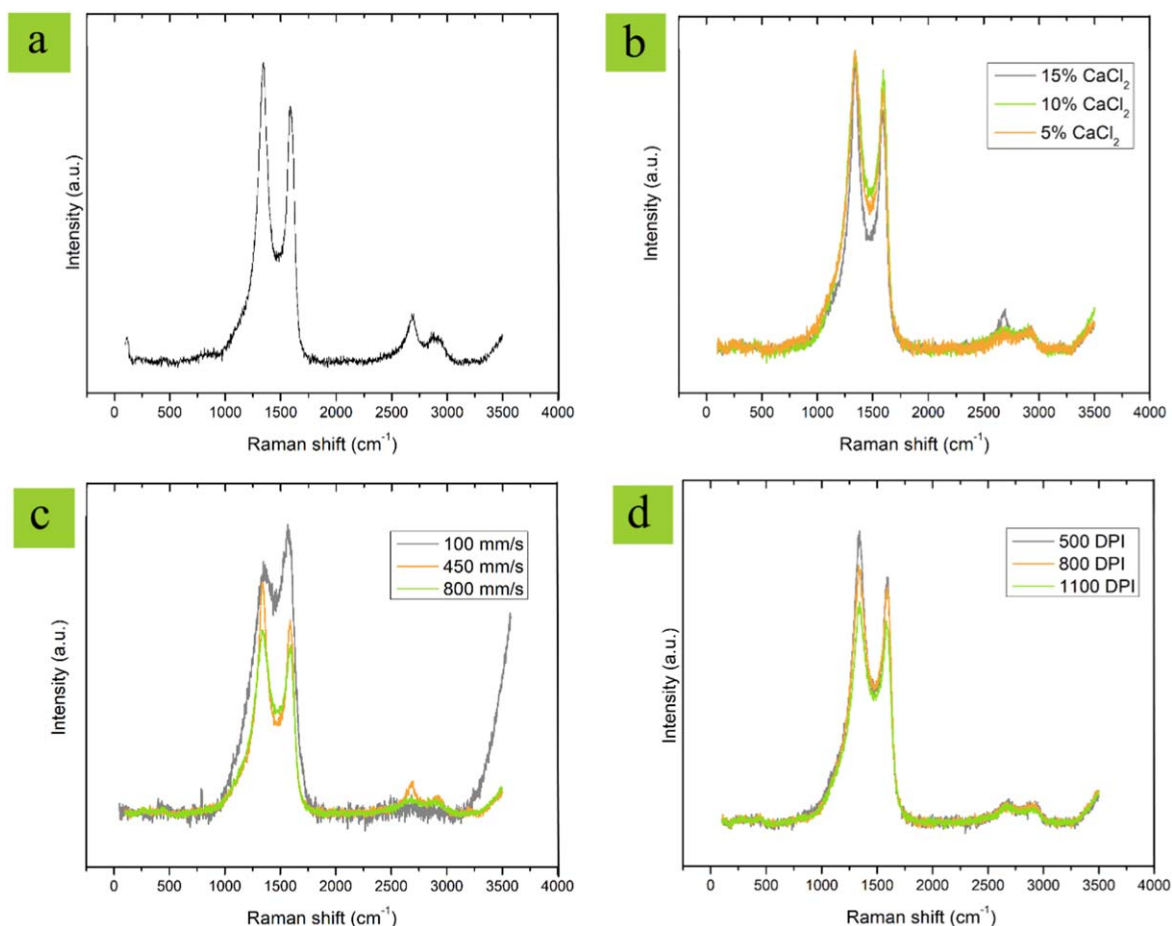


Figure 3. (a) Raman spectrum of LIG obtained with laser power = 14%, scanning speed = 300 mm s^{-1} , and resolution = 1100 DPI on CL-SA with 15% CaCl_2 , (b) LIG on CL-SA with 5%, 10% and 15% CaCl_2 , obtained with laser power = 14%, scanning speed = 450 mm s^{-1} , and resolution = 1100 DPI. (c) LIG on CL-SA with 15% CaCl_2 obtained with laser power = 14% and resolution = 1100 DPI, but different laser scanning speed, and (d) LIG on CL-SA with 15% CaCl_2 obtained with laser power = 14% and scanning speed = 500 mm s^{-1} , but different resolution.

Table 1. Laser parameters used to produce LIG on CL-SA.

| Sample | % CaCl_2 | Speed (mm s^{-1}) | Resolution (DPI) | Sample | % CaCl_2 | Speed (mm s^{-1}) | Resolution (DPI) |
|--------|-------------------|------------------------------|------------------|--------|-------------------|------------------------------|------------------|
| 1 | 5 | 350 | 1100 | 11 | 5 | 500 | 700 |
| 2 | 5 | 400 | 1100 | 12 | 5 | 500 | 900 |
| 3 | 5 | 450 | 1100 | 13 | 5 | 500 | 1300 |
| 4 | 10 | 300 | 1100 | 14 | 10 | 500 | 1000 |
| 5 | 10 | 600 | 1100 | 15 | 10 | 500 | 1200 |
| 6 | 10 | 900 | 1100 | 16 | 10 | 500 | 1400 |
| 7 | 15 | 100 | 1100 | 17 | 15 | 500 | 500 |
| 8 | 15 | 450 | 1100 | 18 | 15 | 500 | 800 |
| 9 | 15 | 600 | 1100 | 19 | 15 | 500 | 1100 |
| 10 | 15 | 750 | 1100 | 20 | 15 | 800 | 1100 |

scanning speed, the lowest FWHM values for both peaks are observed at a medium speed of 450 mm s^{-1} . The high FWHM values for the G and D peaks at the lowest scanning speed (100 mm s^{-1}) suggest the presence of amorphous or disordered material. In contrast, the laser scanning resolution does not play a significant effect on the FWHM of G and D peaks within the chosen resolution range. According to the conducted Raman spectroscopy study, we observe that the

scanning speed of 300 mm s^{-1} and laser resolution of 1100 DPI represent optimal laser parameters for producing LIG on CL-SA.

It is instructive to observe the evolution of the 2D peak with varying cross-linker content, laser scanning speed and resolution. Figure S4 depicts the evolution of the position of this peak as a function of the mentioned three parameters. Taking into account the above discussion, we cannot

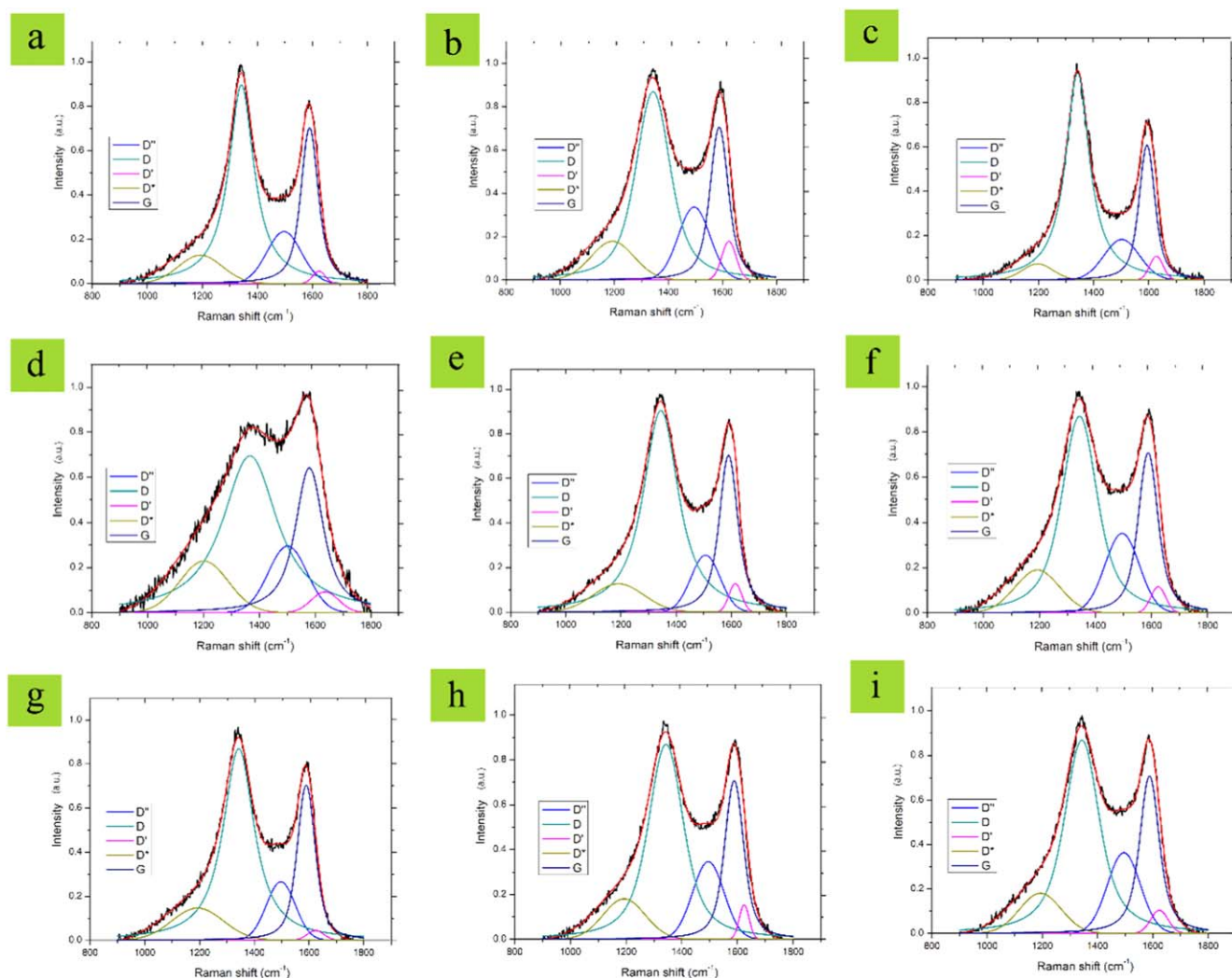


Figure 4. Raman deconvolution for the spectra depicted in figure 3. LIG on CL-SA obtained with laser power = 14%, scanning speed = 450 mm s^{-1} , and resolution = 1100 DPI, with (a) 5% CaCl_2 , (b) 10% CaCl_2 , and (c) 15% CaCl_2 . LIG on CL-SA with 15% CaCl_2 obtained with laser power = 14%, resolution = 1100 DPI and laser scanning speed (d) 100 mm s^{-1} , (e) 450 mm s^{-1} , and (f) 800 mm s^{-1} . LIG on CL-SA with 15% CaCl_2 obtained with laser power = 14%, laser scanning speed = 500 mm s^{-1} and resolution (g) 500 DPI, (h) 800 DPI, and (i) 1100 DPI.

conclude that an increase in crystallinity necessarily leads to a red or blue shift of the 2D peak. In fact, it has been shown before that both doping [38] and strain [39] can induce a shift of the 2D peak. In our case, the oxygen content of LIG changes with changing laser parameters, as does the strain, due to different thermal expansion coefficients of the LIG and the precursor substrate. Since both the oxygen content and the strain change simultaneously, it is difficult to claim what is the exact cause of the shift in 2D peak position.

3.2. FTIR spectroscopy

The FTIR spectra of CL-SA with different calcium chloride content are depicted in figure 6(a). The characteristic peaks of CL-SA appear at 1670 cm^{-1} and 1440 cm^{-1} due to asymmetric and symmetric stretching vibrations of COO^- groups, respectively [40–42]. The broad peak at $\sim 3560 \text{ cm}^{-1}$ corresponds to the stretching vibration of the O–H group [43, 44]. The presence of the 1180 cm^{-1} band may be due to the

elongation of C–O groups [45]. These vibrations are visible regardless of the content of CaCl_2 . To observe the changes in chemical bonds in the substrate or the appearance of new bonds upon laser irradiation, FTIR spectra of LIG on CL-SA were taken, and are shown in figure 6(b). The FTIR spectrum of LIG manifests the –OH stretching vibration as a broad peak at 3400 cm^{-1} , symmetric and asymmetric CH_2 stretching vibrations at 2950 and 2873 cm^{-1} , C=O vibrations of carboxylic groups at 1385 cm^{-1} and 1700 cm^{-1} , the presence of the C=C skeleton at 1690 cm^{-1} and C–O vibrations at 1491 cm^{-1} [46–49]. The –OH stretching vibration of LIG shifts to lower wavelengths compared to pure CL-SA, indicating the interaction of GO and ‘non-converted’ CL-SA molecules through intermolecular hydrogen bonds [50].

Spectra of LIG produced at various laser scanning speeds are shown in figure 6(c). It is noticeable that the intensity of CH_2 stretching bands decreases as scanning speed increases. This commonly happens when CL-SA molecules and Ca^{2+} ions crosslink, forming the ‘egg-box’ structures that limit the

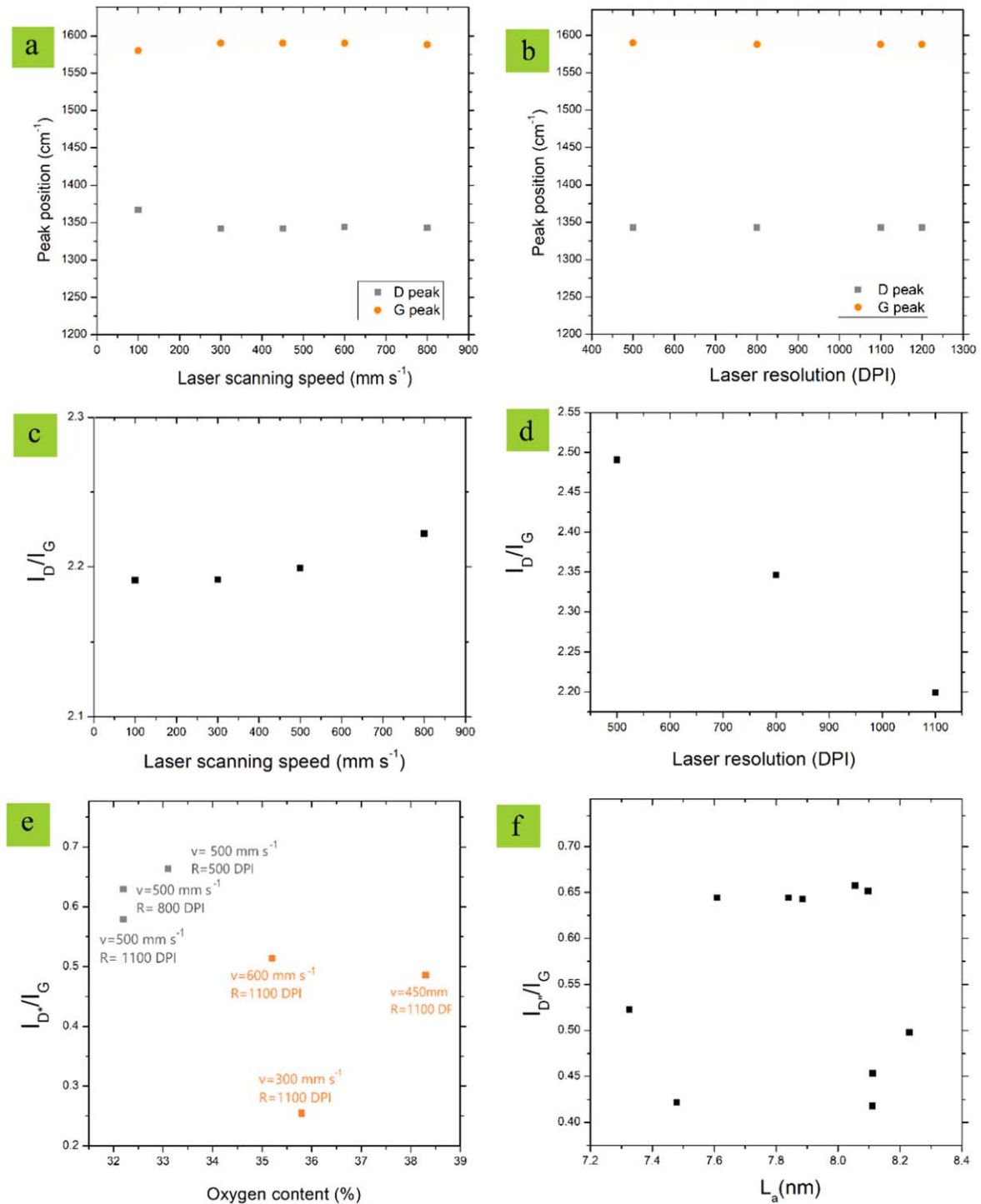


Figure 5. (a) Dependence of the D and G bands position with the laser scanning speed. (b) Dependence of the D and G bands position with the laser resolution. (c) Variation of the I_D/I_G versus the laser scanning speed. (d) Variation of the I_D/I_G versus the laser resolution. (e) I_{D^*}/I_G evolution with the oxygen content. (f) The I_{D^*}/I_G variation versus L_a .

C-H stretching and weaken the peak at 2900 cm^{-1} [20–22]. However, this peak is visible when laser parameters are optimized, as demonstrated in figure 6(c). With specific values of laser speed (450 mm s^{-1}) and resolution (1100 DPI), this peak is well-developed, indicating a successful conversion of CL-SA to LIG. At higher speeds, the conversion is not efficient due to the laser spot moving too fast, while at lower speeds the samples degrade because of

longer local irradiation of the surface. In the region from 2700 to 1700 cm^{-1} , it is evident that the intensity of peaks associated with CL-SA decreases in the case of correctly chosen parameters. In the end, in the region from 1700 to 400 cm^{-1} , all the characteristic peaks shown in figure 6(b) can be observed, when optimal laser parameters are used.

FTIR spectra of LIG produced with different laser resolution are depicted in figure 6(d). CH_2 stretching bands are

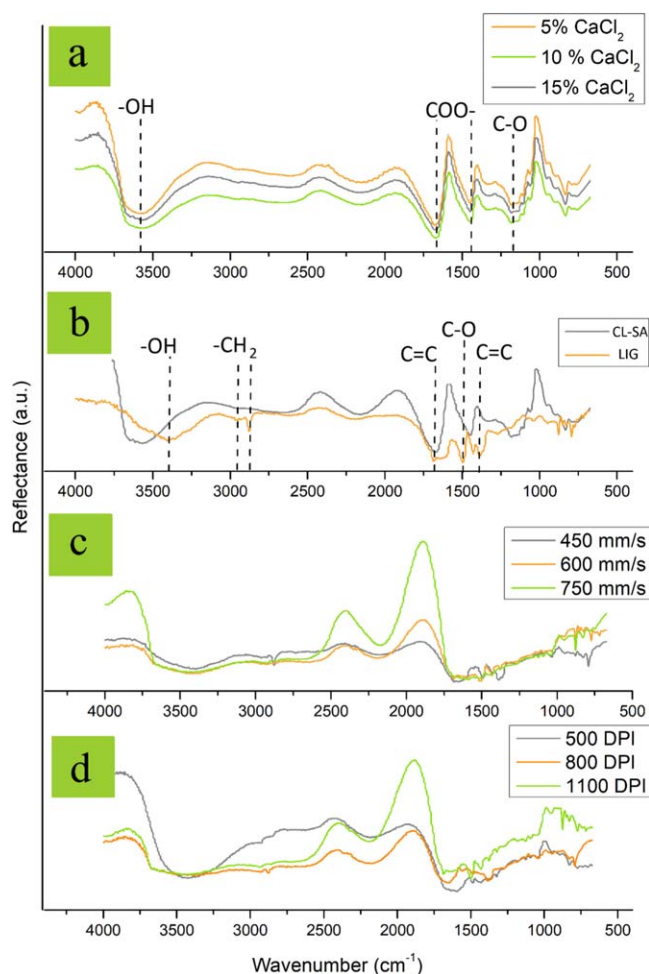


Figure 6. FTIR spectra of CL-SA and LIG. (a) FTIR spectra of pure CL-SA with 5%, 10%, and 15% CaCl_2 . (b) FTIR spectra of CL-SA with 10% CaCl_2 and LIG obtained with laser power = 14%, laser scanning speed = 300 mm s^{-1} , and laser resolution = 1100 DPI. (c) Compared spectra of samples obtained with laser power = 14%, laser resolution = 1100 DPI and laser scanning speeds 450, 600, and 750 mm s^{-1} . (d) Compared spectra of samples obtained with laser power = 14%, laser scanning speed = 500 mm s^{-1} , and laser resolutions 500, 800, and 1100 DPI.

most visible at a resolution of 800 DPI. In the region from 2700 to 1700 cm^{-1} , the peaks associated with CL-SA decrease in intensity with the appropriate parameters. When the resolution exceeds 500 DPI, the peaks in the region from 1700 to 650 cm^{-1} become more prominent, indicating graphene formation. As with Raman spectroscopy, FTIR analysis reveals that low speed and high resolution are favorable conditions for LIG formation.

3.3. SEM-EDS analysis

In order to investigate the effect of laser parameters on the surface morphology and elemental composition, SEM with energy dispersive x-ray analysis (SEM-EDS) was performed on LIG samples produced with various sets of parameters. Figures 7 and 8 depict scanning electron micrographs of the LIG. Pronounced micro-scale pores are evident inside the carbonized structure. At SEM micrographs at $20\,000\times$

magnification it becomes visible that carbon sheets form channel-like structures perpendicular to the substrate surface (marked in figure 8(f)). This occurrence can be attributed to the rapid pyrolysis and carbonization of the CL-SA film caused by localized laser heating. The produced pyrolysis gases are discharged, causing a reorientation of the graphitic and graphene sheets and resulting in the formation of vertically aligned channel networks [51]. To examine the influence of laser speed on the formation of the graphene network, the resolution was kept constant at 1100 DPI. Figure 7 displays surface morphologies of four LIG samples produced with different laser scanning speed. It is evident that lower scanning speed results in better-formed graphene networks, i.e. graphene with more pores. To examine the effect of laser resolution on the formation of the graphene networks, we maintained laser power and laser speed at fixed values of 14% and 500 mm s^{-1} , respectively. Figure 8 displays surface morphologies of four LIG samples generated using four different laser resolutions. Higher resolution yields LIG of a denser microstructure, resulting in more conductive pathways [52]. The effects of such tuned microstructure on electrical resistance will be discussed in subsequent sections.

The same samples were used to analyze the elemental composition of the resulting LIG structures. Table 2 provides the elemental composition of the samples induced with different laser parameters. EDS analysis reveals the presence of carbon, oxygen, calcium and chlorine. To investigate the proportions of these elements in the samples induced with moderate laser scanning speed and resolution, we conducted a systematic study. In order to investigate the effect of speed, laser power and resolution were fixed to 14% and 1100 DPI, respectively. The results indicate that the elemental composition does not vary significantly with scanning speed, within the chosen optimal range of speeds. A fixed laser scanning speed of 500 mm s^{-1} was employed to investigate the impact of scanning resolution. Samples with laser resolution equal to or greater than 800 DPI exhibited slightly higher carbon content. In any of the investigated cases, we find a high O/C ratio, suggesting heavily oxidized LIG being produced on the CL-SA films.

3.3.1. XRD analysis. The XRD patterns of SA and LIG on SA are depicted in figure S5. LIG produced on a 10% SA substrate with 14% laser power, 300 mm s^{-1} scanning speed and a resolution of 900 DPI is chosen for this measurement. The pattern shows a prominent peak at $2\theta = 26.5^\circ$, which corresponds to the (002) plane of LIG. Additionally, there is a peak at $2\theta = 43^\circ$, indexed to (100) reflections associated with an in-plane structure [14, 52]. The inter-planar distance (d) can be calculated using Bragg's equation $n\lambda = 2d\sin\theta$. For the first diffraction order ($n = 1$), x-ray wavelength of 1.54 \AA , and an incident angle (θ) of 13.25° , the calculated value of the inter-planar distance between (002) planes is 3.4 \AA , which is in accordance with the literature data [53]. Reflections

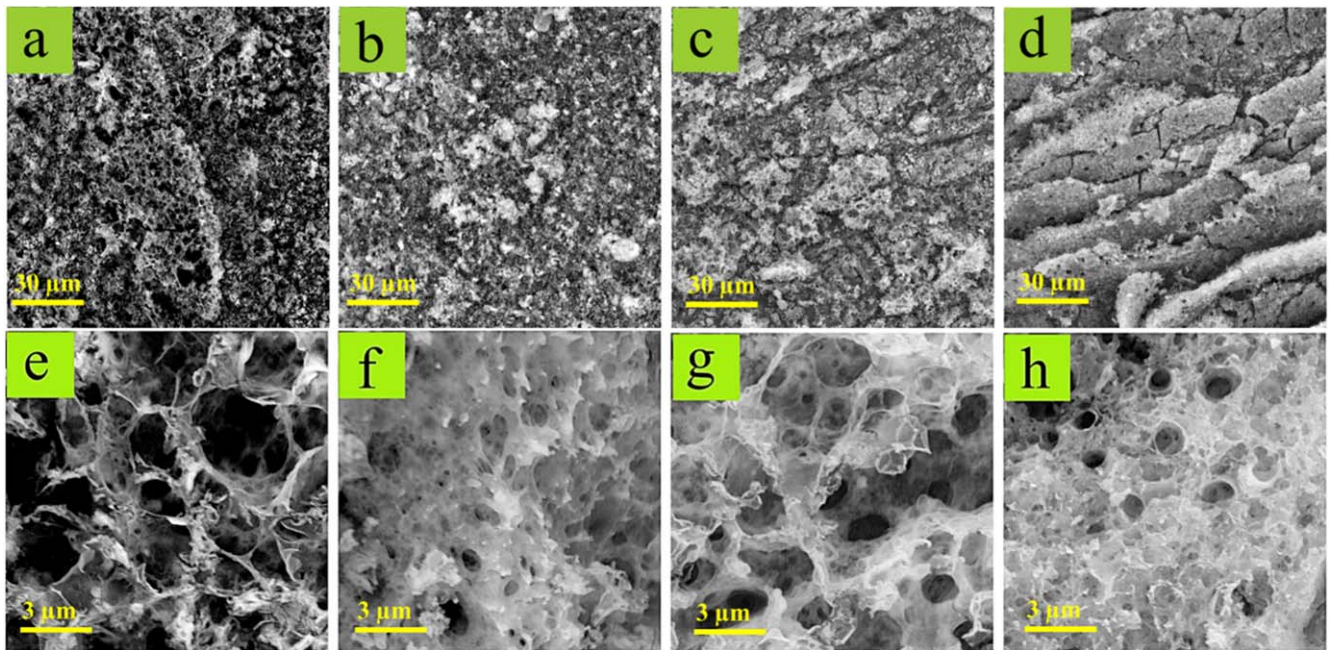


Figure 7. SEM images of LIG on CL-SA with 15% CaCl_2 at magnification $2000\times$. Laser parameters include power = 14%, resolution = 1100 DPI, and scanning speed: (a) 300 mm s^{-1} , (b) 450 mm s^{-1} , (c) 600 mm s^{-1} , (d) 750 mm s^{-1} . SEM images of LIG on CL-SA at magnification $20\,000\times$. Laser parameters include power = 14%, resolution = 1100 DPI, and scanning speed: (e) 300 mm s^{-1} , (f) 450 mm s^{-1} , (g) 600 mm s^{-1} , and (h) 750 mm s^{-1} .

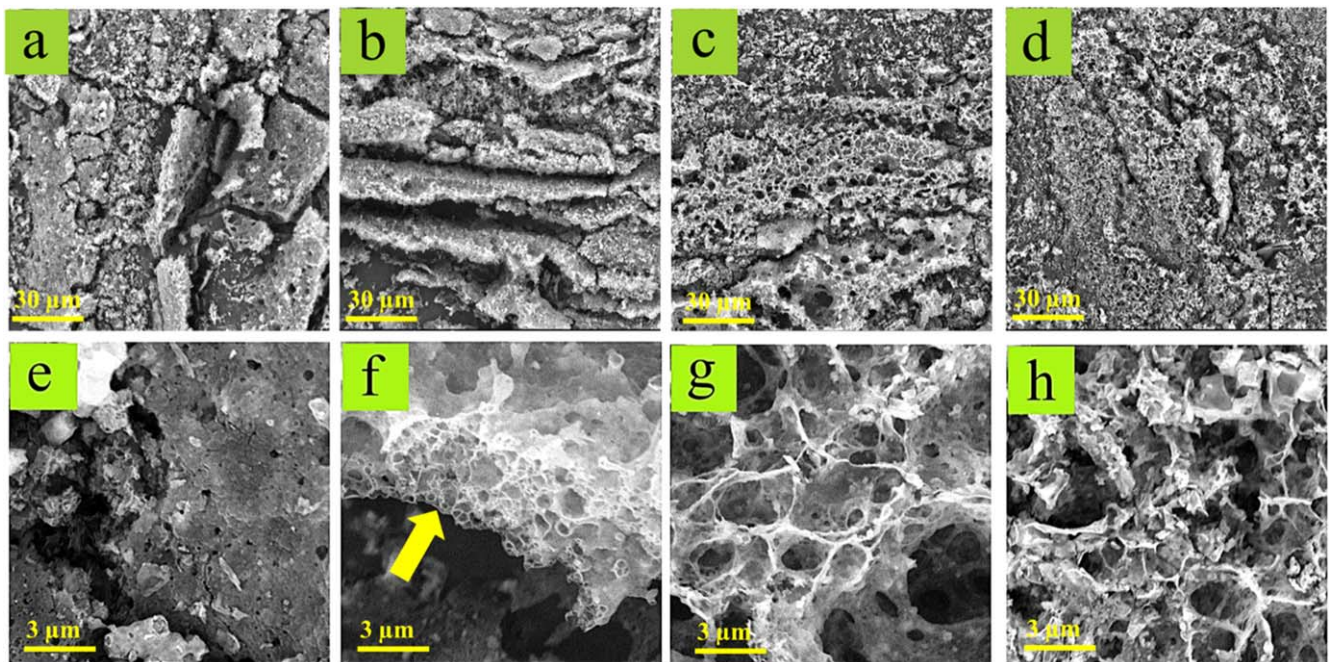


Figure 8. SEM images of LIG on CL-SA with 15% CaCl_2 at magnification $2000\times$. Laser parameters include power = 14%, speed = 500 mm s^{-1} , and resolution: (a) 500 DPI, (b) 800 DPI, (c) 1100 DPI, and (d) 1400 DPI. SEM images of LIG on CL-SA at magnification $20\,000\times$. Laser parameters include power = 14%, scanning speed = 500 mm s^{-1} , and resolution: (e) 500 DPI, (f) 800 DPI, (g) 1100 DPI, and (h) 1400 DPI.

Table 2. Elemental composition of the samples produced with different laser parameters, as obtained with EDS.

| Speed (mm s ⁻¹) | Resolution (DPI) | C (%) | O (%) | Ca (%) | Cl (%) |
|--------------------------------|---------------------|-------|-------|--------|--------|
| 300 | 1100 | 59.7 | 35.8 | 3.8 | 0.7 |
| 450 | 1100 | 56.6 | 38.3 | 3.6 | 1.5 |
| 600 | 1100 | 57.9 | 35.2 | 5.5 | 1.4 |
| 750 | 1100 | 60.2 | 35.6 | 3.5 | 0.7 |
| 500 | 500 | 61.4 | 33.1 | 4.2 | 1.3 |
| 500 | 800 | 63.6 | 32.2 | 3.9 | 0.3 |
| 500 | 1100 | 63.3 | 32.2 | 3.7 | 0.8 |
| 500 | 1400 | 63.2 | 32.5 | 3.6 | 0.7 |

occurring at $2\theta = 30.5^\circ$ and $2\theta = 33^\circ$ originate from vaterite CaCO_3 crystals formed on the surface during laser irradiation.

3.4. TEM analysis

TEM reveals (figure 9) a surface with randomly oriented domains appearing as groups of parallel lines. The spacing between intensity maxima of the parallel lines translates to interlayer spacing of 0.34 nm, which is the value expected for graphene, and is consistent with results obtained with XRD (see supplementary information) [53, 54]. Figure 9(c) illustrates the EDS maps of carbon and oxygen, confirming the predominant presence of carbon atoms.

3.5. XPS analysis

The impact of the scanning speed and the CaCl_2 content on the formation of LIG has been demonstrated with previously mentioned techniques. To investigate the influence of these parameters on the surface chemical composition of the formed LIG, XPS was employed. Two samples with different CaCl_2 content, produced with different scanning speeds, were selected for analysis. In particular, we chose substrates with 15% and 10% CaCl_2 , while the laser power and resolution were fixed at 14% and 1100 DPI, respectively. The scanning speed was set at 700 mm s^{-1} for the first sample and 350 mm s^{-1} for the second sample. Survey spectra of CL-SA with 10% and 15% CaCl_2 are depicted in figure S6. Figure 10(a) depicts XPS survey spectra of both samples, revealing the presence of C, O, Ca, and Cl, as also observed with EDS. High-resolution C 1s spectra of the LIG samples, shown in figure 10(b) were deconvoluted into five peaks. The major functionalities observed were sp^2 carbon bonds ($\sim 284.3 \text{ eV}$), sp^3 carbon bonds ($\sim 284.9 \text{ eV}$), C–OH ($\sim 286.2 \text{ eV}$), O–C–O ($\sim 288.0 \text{ eV}$), and O–C=O ($\sim 288.5 \text{ eV}$) [55–58]. The sp^2 carbon atom hybridization percentages of both LIG samples exhibit similar values. The elemental composition determined with XPS is presented in table 3. It is evident that the chemical composition of the LIG does not change with linker concentration and laser scanning speed. The results of characterization with the different presented methods reveal a plethora of information about the material at hand. XPS data (figure 10 and table 3) confirm the presence of sp^2

hybridization in the carbon lattice, which indicates the formation of graphene. The same data, however, also indicate sp^3 hybridization, which indicates that other allotropes of carbon are still present in the sample. The ratio of sp^2 to sp^3 does not unambiguously change with changing cross-linker concentration. EDS analysis, presented in table 2, shows a high content of carbon in all samples, although it also points to a strong presence of oxygen, which, together with XPS results, indicates the presence of some degree of graphene oxide in all samples. Finally, the efficiency of graphenization can be related to the prominence of graphene-related peaks in Raman spectra, such as G and D peaks, against a non-graphene background. Figure S2 (Supporting Information) depicts the same Raman spectra that are shown in figure 4, but without correction for the fluorescence background. In agreement with results from XPS, it cannot be conclusively stated that increasing cross-linker concentration from 5% to 15% leads to a higher degree of graphitization. It is, however, evident that changing the scanning speed from 100 to 400 mm s^{-1} does lead to increased prominence of G and D peaks, and a suppression of fluorescence background, which indicates better graphitization at 400 mm s^{-1} . Further increasing the scanning speed to 800 mm s^{-1} has no effect on the degree of graphitization. Similarly, increasing laser scanning resolution from 500 DPI to 800 DPI and 1100 DPI does lead to progressive improvement of the degree of graphitization with increasing resolution. Such results have been observed before in the case of laser-induced graphenization of textile yarn [59].

3.6. Electrical resistance measurements

Figure 11 displays the electrical resistances of the samples listed in table 1. We evaluated the impact on electrical resistance of varying laser scanning speed and resolution, for all three concentrations of CaCl_2 . From figure 11(a) it is apparent that for all three concentrations of the cross-linker, measured resistance increases with increasing scanning speed. This is not surprising, given that at higher speeds the laser spends less time converting the CL-SA to LIG. The increase of resistance with scanning speed is especially apparent in the case of 5% concentration of CaCl_2 , which could indicate poor CL-SA crosslinking at CaCl_2 concentrations smaller than 10%. We believe that the resistance variations are primarily due to the efficiency of cross-linking and not the degree of oxidation, as oxygen content does not vary significantly among the samples (tables 2 and 3). Figure 11(b) depicts the dependence of electrical resistance on laser resolution. The data indicate a decrease of resistance with increasing laser resolution regardless of the concentration of cross-linker. The results indicate that the combination of low laser scanning speed, high resolution and higher CaCl_2 content is required if a low resistance is desired when creating LIG on CL-SA. Varying the laser parameters offers a facile route to tuning electrical resistance of the obtained structures. Based on the results depicted in figure 11, we conclude that the combination of parameters that yields the lowest sheet resistance,

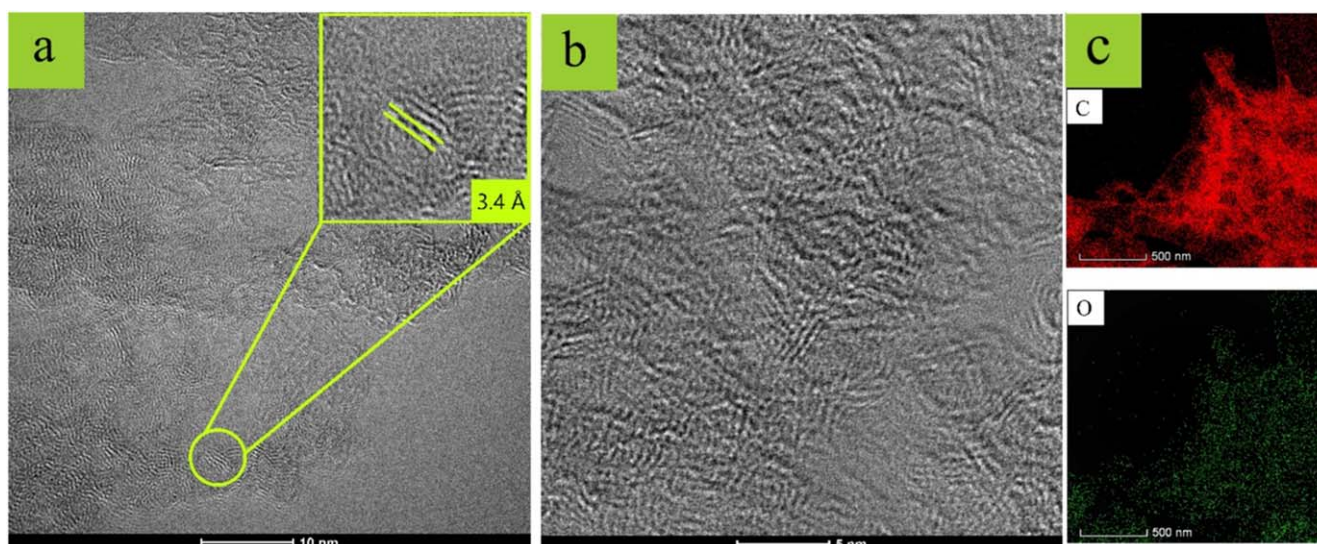


Figure 9. TEM image of LIG on CL-SA. Randomly oriented domains of graphene are seen as groups of parallel lines. (a) 10 nm scale, (b) 5 nm scale, (c) carbon (red) and oxygen (green) EDS maps.

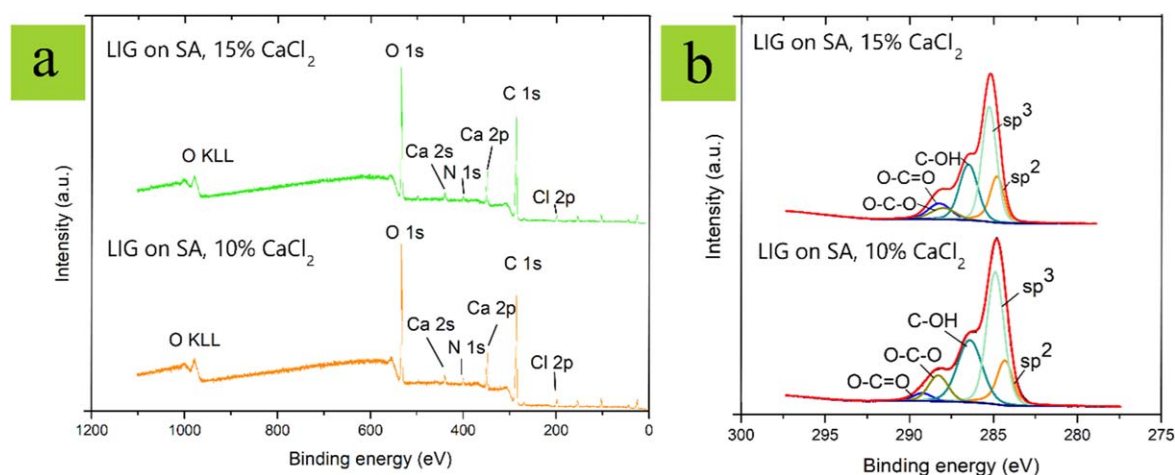


Figure 10. XPS spectra. (a) Survey spectra of LIG on CL-SA with 15% CaCl_2 and applied laser scanning speed of 700 mm s^{-1} (green) and LIG on CL-SA with 10% CaCl_2 and applied laser scanning speed of 350 mm s^{-1} (orange). (b) High resolution C 1s spectra.

Table 3. Elemental composition determined by XPS.

| Bond | LIG on CL-SA (10% CaCl_2) | LIG on CL-SA (15% CaCl_2) |
|-------------|-------------------------------------|-------------------------------------|
| C 1s (at%) | 67.7 | 68.0 |
| O 1s (at%) | 27.2 | 27.0 |
| Ca 2p (at%) | 3.6 | 3.6 |
| Cl 2p (at%) | 1.5 | 1.4 |

among the parameters examined, is achieved with a laser scanning speed of 300 mm s^{-1} and a resolution of 1400 DPI. LIG obtained from the commonly used polymer polyimide exhibits average sheet resistance values of $50 \Omega \text{ sq}^{-1}$. While LIG samples based on sodium alginate exhibit higher sheet resistance, they can still find utility in applications where moderate conductivity suffices or in scenarios where other attributes such as biocompatibility take precedence. Considering that the conductivity of oxidized graphene is highly

dependent on the oxidation degree and that the oxidation degree can be relatively easily tuned electrochemically [60], precise and broad control of conductivity may be possible by combining electrochemical and laser tuning. Moreover, the inherent biocompatibility of alginate hydrogels, when combined with their controllable resistance properties, presents a compelling avenue for implementation in the realm of nanobiotechnology.

4. Conclusion

LIG formation on CL-SA has been systematically studied in this work. Physicochemical characterization of the resulting LIG was conducted, including Raman spectroscopy, SEM-EDS, XRD, TEM, FTIR and XPS. All methods demonstrate formation of graphene on the surface of CL-SA. The effect of laser parameters and the amount of crosslinker added to the CL-SA substrate have also been investigated. The results

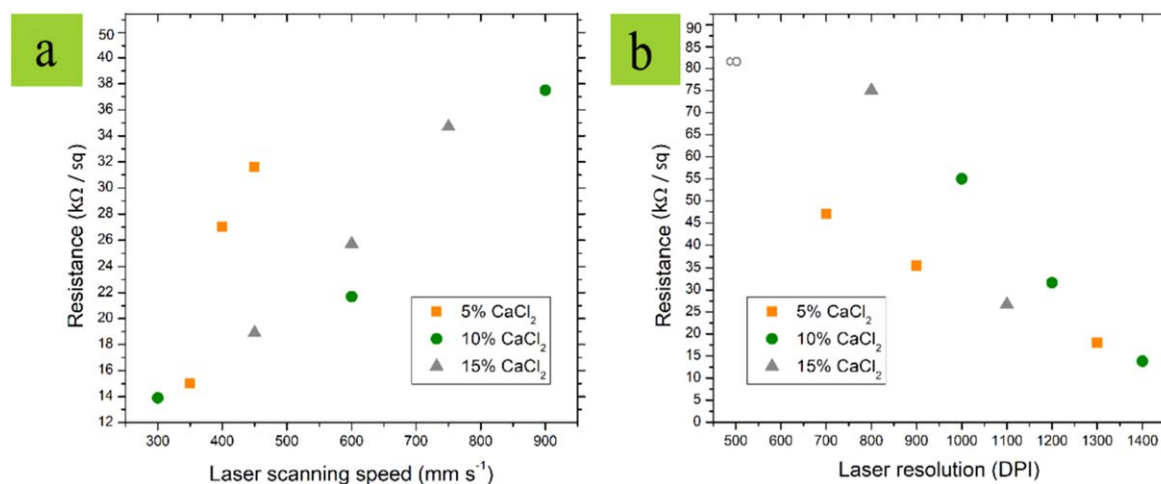


Figure 11. Measured electrical resistance of LIG produced with different laser parameters and with different concentrations of CaCl₂. (a) Electrical resistance of samples produced with varying laser scanning speed. (b) Electrical resistance of samples produced with varying laser resolution.

show that the combination of low laser scanning speed, high resolution, and higher CaCl₂ content is required when creating LIG from CL-SA with a desired low resistance. LIG on CL-SA has potential applications in bioelectronics, including medical wearables. The remarkable biocompatibility of alginate hydrogels further augments the appeal of this hybrid system, offering a platform that seamlessly integrates controllable resistance with the biocompatibility required for interfacing with biological systems. Assessing the properties of LIG derived from different polymers, it is clear that the choice of the polymeric precursor plays a crucial role in the characteristics of the resulting graphene material. Namely, LIG obtained from the commonly used polymer polyimide exhibits excellent electrical conductivity, thermal stability and flexibility. On the other hand, sodium alginate-based LIG may exhibit lower conductivity but can still be utilized in applications where moderate conductivity is sufficient or where other properties like biocompatibility are prioritized.

Acknowledgments

TV, MS, IG and CSI acknowledge the support provided by the NATO Science for Peace and Security Program under project SP4LIFE, number G5825. DBB and IAP acknowledge the support provided by the Serbian Ministry of Science, Technological Development, and Innovations (contract number: 451-03-47/2023-01/200146). We also acknowledge support by the Serbian Ministry of Science, Technological Development, and Innovations, contract number 451-03-47/2023-01/200026. IAP is also indebted to the Research Fund of the Serbian Academy of Sciences and Arts, project F-190, for supporting this study. GSD acknowledges the support provided by dtec.bw – Digitalization and Technology Research Center of the Bundeswehr for support [project VITAL-SENSE]. dtec.bw is funded via the German Recovery and Resilience Plan by the European Union (NextGenerationEU).

Data availability statement

All data that support the findings of this study are included within the article (and any supplementary files).

Conflicts of interest

The authors declare no conflict of interest.

ORCID iDs

T Vičentić <https://orcid.org/0000-0002-3460-6137>

I Greco <https://orcid.org/0009-0009-7471-7032>

C S Iorio <https://orcid.org/0000-0003-0952-0064>

V Mišković <https://orcid.org/0000-0003-1475-0243>

D Bajuk-Bogdanović <https://orcid.org/0000-0003-2443-376X>

I A Pašti <https://orcid.org/0000-0002-1000-9784>

T Stimpel-Lindner <https://orcid.org/0000-0002-4864-4898>

G S Duesberg <https://orcid.org/0000-0002-0155-2558>

M Spasenović <https://orcid.org/0000-0002-2173-0972>

References

- [1] Novoselov K S, Geim A K, Morozov S V, Jiang D, Zhang Y, Dubonos S V, Grigorieva I V and Firsov A A 2004 Electric field effect in atomically thin carbon films *Science* **306** 666–9
- [2] Novoselov K S, Jiang D, Schedin F, Booth T J, Khotkevich V V, Morozov S V and Geim A K 2005 Two-dimensional atomic crystals *Proc. Natl. Acad. Sci. USA* **102** 10451–3
- [3] Li X *et al* 2009 Large-area synthesis of high-quality and uniform graphene films on copper foils *Science* **324** 1312–4
- [4] Reina A, Jia X, Ho J, Nezich D, Son H, Bulovic V, Dresselhaus M S and Jing K 2009 Large area, few-layer

- graphene films on arbitrary substrates by chemical vapor deposition *Nano Lett.* **9** 30–5
- [5] Kim K S, Zhao Y, Jang H, Lee S Y, Kim J M, Kim K S, Ahn J H, Kim P, Choi J Y and Hong B H 2009 Large-scale pattern growth of graphene films for stretchable transparent electrodes *Nature* **457** 706–10
- [6] Hernandez Y et al 2008 High-yield production of graphene by liquid-phase exfoliation of graphite *Nat. Nanotechnol.* **3** 563–8
- [7] Lotya M et al 2009 Liquid phase production of graphene by exfoliation of graphite in surfactant/water solutions *J. Am. Chem. Soc.* **131** 3611–20
- [8] Bourlinos A B, Georgakilas V, Zboril R, Steriotis T A, Stubos A K and Trapalis C 2009 Aqueous-phase exfoliation of graphite in the presence of polyvinylpyrrolidone for the production of water-soluble graphenes *Solid State Commun.* **149** 2172–6
- [9] Lotya M, King P J, Khan U, De S and Coleman J N 2010 High-concentration, surfactant-stabilized graphene dispersions *ACS Nano* **4** 3155–62
- [10] Park S and Ruoff R S 2009 Chemical methods for the production of graphenes *Nat. Nanotechnol.* **4** 217–24
- [11] Hummers W S and Offeman R E 1958 Preparation of graphitic oxide *J. Am. Chem. Soc.* **80** 1339
- [12] Bhorkar K, Samartzis N, Athanasiou M, Sygellou L, Boukos N, Dracopoulos V, Ioannides T and Yannopoulos S N 2022 Laser-assisted explosive synthesis and transfer of turbostratic graphene-related materials for energy conversion applications *npj 2D Mater. Appl.* **6** 1–13
- [13] Praeger M, Papazoglou S, Pesquera A, Zurutuza A, Levi A, Naveh D, Zergioti I, Eason R W and Mills B 2020 Laser-induced backward transfer of monolayer graphene *Appl. Surf. Sci.* **533** 147488
- [14] Lin J, Peng Z, Liu Y, Ruiz-Zepeda F, Ye R, Samuel E L G, Yacaman M J, Yakobson B I and Tour J M 2014 Laser-induced porous graphene films from commercial polymers *Nat. Commun.* **5** 1–8
- [15] Sun X, Liu X and Li F 2021 Sulfur-doped laser-induced graphene derived from polyethersulfone and lignin hybrid for all-solid-state supercapacitor *Appl. Surf. Sci.* **551** 149438
- [16] Zhu C, Zhao D, Wang K, Dong X, Duan W, Wang F and Gao M 2019 Direct laser writing of graphene films from a polyether ether ketone precursor *J. Mater. Sci.* **54** 4192–202
- [17] Ye R, Peng Z, Wang T, Xu Y, Zhang J, Li Y, Nilewski L G, Lin J and Tour J M 2015 In Situ formation of metal oxide nanocrystals embedded in laser-induced graphene *ACS Nano* **9** 9244–51
- [18] Peng Z, Ye R, Mann J A, Zakhidov D, Li Y, Smalley P R, Lin J and Tour J M 2015 Flexible boron-doped laser-induced graphene microsupercapacitors *ACS Nano* **9** 5868–75
- [19] Ye R, Chyan Y, Zhang J, Li Y, Han X, Kittrell C and Tour J M 2017 Laser-induced graphene formation on wood *Adv. Mater.* **29** 1702211
- [20] Mahmood F, Mahmood F, Zhang H, Lin J and Wan C 2020 Laser-induced graphene derived from Kraft Lignin for flexible supercapacitors *ACS Omega* **5** 14611–8
- [21] Chyan Y, Ye R, Li Y, Singh S P, Arnusch C J and Tour J M 2018 Laser-induced graphene by multiple lasing: toward electronics on cloth, paper, and food *ACS Nano* **12** 2176–83
- [22] Ahmad A et al 2021 A critical review on the synthesis of natural sodium alginate based composite materials: an innovative biological polymer for biomedical delivery applications *Processes* **9** 137
- [23] August A D, Kong H J and Mooney D J 2006 Alginate hydrogels as biomaterials *Macromol. Biosci.* **6** 623–33
- [24] George M and Abraham T E 2006 Polyionic hydrocolloids for the intestinal delivery of protein drugs: alginate and chitosan—a review *J. Control. Release* **114** 1–14
- [25] Sharma S, Sanpui P, Chattopadhyay A and Ghosh S S 2012 Fabrication of antibacterial silver nanoparticle—sodium alginate-chitosan composite films *RSC Adv.* **2** 5837–43
- [26] Lee K Y and Mooney D J 2012 Alginate: properties and biomedical applications *Prog. Polym. Sci.* **37** 106–26
- [27] Vičentić T, Rašljić Rafajilović M, Ilić S D, Koteska B, Madevska Bogdanova A, Pašti I A, Lehocki F and Spasenović M 2022 Laser-induced graphene for heartbeat monitoring with HeartPy analysis *Sensors* **22** 6326
- [28] Chen X, Luo F, Yuan M, Xie D, Shen L, Zheng K, Wang Z, Li X and Tao L Q 2019 A dual-functional graphene-based self-alarm health-monitoring e-skin *Adv. Funct. Mater.* **29** 1904706
- [29] Luo S, Hoang P T and Liu T 2016 Direct laser writing for creating porous graphitic structures and their use for flexible and highly sensitive sensor and sensor arrays *Carbon NY* **96** 522–31
- [30] Stanford M G, Zhang C, Fowlkes J D, Hoffman A, Ivanov I N, Rack P D and Tour J M 2020 High-resolution laser-induced graphene. Flexible electronics beyond the visible limit *ACS Appl. Mater. Interfaces* **12** 10902–7
- [31] Malard L M, Pimenta M A, Dresselhaus G and Dresselhaus M S 2009 Raman spectroscopy in graphene *Phys. Rep.* **473** 51–87
- [32] Ferrari A C et al 2006 Raman spectrum of graphene and graphene layers *Phys. Rev. Lett.* **97** 187401
- [33] Claramunt S, Varea A, López-Díaz D, Velázquez M M, Cornet A and Cirera A 2015 The importance of interbands on the interpretation of the raman spectrum of graphene oxide *J. Phys. Chem. C* **119** 10123–9
- [34] Cañado L G, Takai K, Enoki T, Endo M, Kim Y A, Mizusaki H, Jorio A, Coelho L N, Magalhães-Paniago R and Pimenta M A 2006 General equation for the determination of the crystallite size l_a of nanographite by Raman spectroscopy *Appl. Phys. Lett.* **88** 161101
- [35] Sadezky A, Muckenhuber H, Grothe H, Niessner R and Pöschl U 2005 Raman microspectroscopy of soot and related carbonaceous materials: spectral analysis and structural information *Carbon NY* **43** 1731–42
- [36] Vollebregt S, Ishihara R, Tichelaar F D, Hou Y and Beenakker C I M 2012 Influence of the growth temperature on the first and second-order Raman band ratios and widths of carbon nanotubes and fibers *Carbon NY* **50** 3542–54
- [37] Kaur S, Mager D, Korvink J G and Islam M 2021 Unraveling the dependency on multiple passes in laser-induced graphene electrodes for supercapacitor and H₂O₂ sensing *Mater. Sci. Energy Technol.* **4** 407–12
- [38] Das A et al 2008 Monitoring dopants by Raman scattering in an electrochemically top-gated graphene transistor *Nat. Nanotechnol.* **3** 210–5
- [39] Ni Z H, Yu T, Lu Y H, Wang Y Y, Feng Y P and Shen Z X 2008 Uniaxial strain on graphene: raman spectroscopy study and band-gap opening *ACS Nano* **2** 2301–5
- [40] Sarmiento B, Ferreira D, Veiga F and Nio Ribeiro A 2006 Characterization of insulin-loaded alginate nanoparticles produced by ionotropic pre-gelation through DSC and FTIR studies *Carbohydrate Polym.* **66** 1–7
- [41] Han J, Zhou Z, Yin R, Yang D and Nie J 2010 Alginate-chitosan/hydroxyapatite polyelectrolyte complex porous scaffolds: preparation and characterization *Int. J. Biol. Macromol.* **46** 199–205
- [42] Huang R Y M, Pal R and Moon G Y 1999 Characteristics of sodium alginate membranes for the pervaporation dehydration of ethanol-water and isopropanol-water mixtures *J. Memb. Sci.* **160** 101–13
- [43] Pongjanyakul T 2009 Alginate–magnesium aluminum silicate films: importance of alginate block structures *Int. J. Pharm.* **365** 100–8

- [44] Dong Z, Wang Q and Du Y 2006 Alginate/gelatin blend films and their properties for drug controlled release *J. Memb. Sci.* **280** 37–44
- [45] Pereira R, Tojeira A, Vaz D C, Mendes A and Bártoło P 2011 Preparation and characterization of films based on alginate and aloe vera *Int. J. Polym. Anal. Charact.* **16** 449–64
- [46] Zhu C, Tao L Q, Wang Y, Zheng K, Yu J, L X, Chen X and Huang Y 2020 Graphene oxide humidity sensor with laser-induced graphene porous electrodes *Sensors Actuators B* **325** 128790
- [47] Elahe D and Alireza H 2018 A review on separation techniques of graphene oxide (GO)/base on hybrid polymer membranes for eradication of dyes and oil compounds: recent progress in graphene oxide (GO)/base on polymer membranes-related nanotechnologies *Clin. Med. Rev. Case. Rep.* **5** 228
- [48] Gudarzi M M and Sharif F 2012 Enhancement of dispersion and bonding of graphene-polymer through wet transfer of functionalized graphene oxide *Express Polym. Lett.* **6** 1017–31
- [49] Pourhashem S, Vaezi M R and Rashidi A 2017 Investigating the effect of SiO₂-graphene oxide hybrid as inorganic nanofiller on corrosion protection properties of epoxy coatings *Surf. Coat. Technol.* **311** 282–94
- [50] Xiao C, Liu H, Lu Y and Zhang L 2007 Blend films from sodium alginate and gelatin solutions *J. Macromol. Sci. A* **38** 317–28
- [51] Karimi G, Lau I, Fowler M and Pope M 2021 Parametric study of laser-induced graphene conductive traces and their application as flexible heaters *Int. J. Energy Res.* **45** 13712–25
- [52] Liu M, Wu J N and Cheng H Y 2022 Effects of laser processing parameters on properties of laser-induced graphene by irradiating CO₂ laser on polyimide *Sci. China Technol. Sci.* **65** 41–52
- [53] Cao L, Zhu S, Pan B, Dai X, Zhao W, Liu Y, Xie W, Kuang Y and Liu X 2020 Stable and durable laser-induced graphene patterns embedded in polymer substrates *Carbon NY* **163** 85–94
- [54] Ye R, James D K and Tour J M 2018 Laser-induced graphene *Acc. Chem. Res.* **51** 1609–20
- [55] Kulyk B, Silva B F R, Carvalho A F, Silvestre S, Fernandes A J S, Martins R, Fortunato E and Costa F M 2021 Laser-induced graphene from paper for mechanical sensing *ACS Appl. Mater. Interfaces* **13** 10210–21
- [56] Zhang J, Ren M, Wang L, Li Y, Yakobson B I and Tour J M 2018 Oxidized laser-induced graphene for efficient oxygen electrocatalysis *Adv. Mater.* **30** 1707319
- [57] Chen Y *et al* 2021 Interfacial laser-induced graphene enabling high-performance liquid–solid triboelectric nanogenerator *Adv. Mater.* **33** 2104290
- [58] Garland N T, McLamore E S, Cavallaro N D, Mendivelso-Perez D, Smith E A, Jing D and Claussen J C 2018 Flexible laser-induced graphene for nitrogen sensing in soil *ACS Appl. Mater. Interfaces* **10** 39124–33
- [59] Parmeggiani M, Stassi S, Fontana M, Bianco S, Catania F, Scaltrito L and Lamberti A 2021 Laser-induced graphenization of textile yarn for wearable electronics application *Smart Mater. Struct.* **30** 105007
- [60] Karačić D, Gutić S J, Vasić B, Mirsky V M, Skorodumova N V, Mentus S V and Pašti I A 2022 Electrochemical reduction of thin graphene-oxide films in aqueous solutions—restoration of conductivity *Electrochim. Acta* **410** 140046